

Different Cold Spray Deposition Strategies: Single- and Multi-layers to Repair Aluminium Alloy Components

Silvano Rech, Andrea Trentin, Simone Vezzù, Enrico Vedelago, Jean-Gabriel Legoux, and Eric Irissou

(Submitted July 23, 2013; in revised form March 25, 2014)

Cold spraying is increasingly being used for reconstruction or repair of damaged aluminium alloy components, especially in the aviation industry. Both thin (<0.5 mm) and thick (up to 1 cm) coatings are necessary to achieve dimensional recovery of such components. Thin and above all thick coatings can be deposited in a single pass (single layer) or in several passes (multi-pass), resulting in different thermal and stress effects in the component and the coating itself. The thermal input, the amount and type of residual stresses and the porosity affect various characteristics such as adhesion, crack propagation and mechanical properties of the coating. In this study, two sets (single- and multi-pass) of aluminium alloy (AA6061) coatings with different thicknesses (0.5 mm to 2 mm) were deposited onto AA6061 substrates and compared using metallographic and fractographic analyses, four-point bending testing, residual stress analysis and Vickers microhardness indentation. Finally, the coating adhesion and cohesion were measured using the standard ASTM-C633 adhesion test and tubular coating tensile test. This study demonstrates that the single-layer strategy results in greater adhesion and lower porosity, while multi-layer coatings have higher elastic modulus. Independent of the strategy, the compressive residual stress decreases as a function of coating thickness.

Keywords aircraft, feedstock, processing, testing

1. Introduction

Military rotorcraft transmission housings and gearboxes of military and civil aircraft are made of magnesium or aluminium alloys, and polymer injection moulds made from aluminium alloys can be affected by construction defects (casting defects, porosity) or damage during service (erosion and abrasion). Such defects can be restored by cold spraying (Ref 1-3). The cold spray repair process has been demonstrated to be economically advantageous (Ref 4), and it can be incorporated into a repair facility or as part of production (Ref 5).

Welding (Ref 6) and lasers (Ref 7) are widely used for component restoration, but thermal residual stress and deformation resulting from the solidification of the melted material caused by the high thermal input (Ref 8) can degrade the quality of the repaired part (Ref 9), giving rise to a

short lifecycle of (low-melting magnesium or aluminium alloy) restored components. Cold-sprayed aluminium coatings have low compressive residual stress (Ref 10) and very low thermal input and cause no microstructural changes in the base alloy (Ref 11). These properties make cold spraying a competitive technology for repair not only in terms of cost and industrialization but also in terms of performance.

In a previous work (Ref 12), the presence of tensile stress peaks at interfaces between sequential layers of a multilayer coating was identified, providing the motivation to investigate whether other mechanical and structural coating properties could vary with the deposition strategy, in particular with the number of layers for the same coating thickness. Therefore, the present study is a continuation of the previous study, focussing on evaluation of microstructural and mechanical properties of cold-sprayed aluminium alloy (AA6061) coatings deposited on substrates of the same alloy using single-pass (single layer) and multi-pass (layer upon layer) deposition. In addition, coatings exhibiting different thicknesses obtained by a single spray pass were investigated to understand how thickness influences coating properties.

Both methodologies are valid alternatives to achieve high coating thickness, so it is important to know the structural properties and requirements of the respective coatings in order to perform restoration suitable for a particular damaged component.

2. Experimental Procedures

The powder sprayed in this study was gas-atomized aluminium alloy 6061 (magnesium-silicon aluminium alloy;

This article was presented at the 2011 International Thermal Spray Conference in Hamburg, Germany, September 27–29, 2011, and has been expanded from the original presentation.

Silvano Rech, Andrea Trentin, Simone Vezzù, and Enrico Vedelago, Veneto Nanotech, Via delle Industrie 12, 30175 Marghera, Italy; and **Jean-Gabriel Legoux and Eric Irissou**, Industrial Materials Institute (IMI), National Research Council Canada (NRC-NRC), 75 de Mortagne Boulevard, Boucherville, QC J4B 6Y4, Canada. Contact e-mail: silvano.rech@venetonanotech.it.

TLS Technik GmbH, KG, D-06733 Bitterfeld, Germany), with particle size ranging between 5 and 50 μm (as reported by the supplier). The powder inductively coupled plasma (ICP) analysis provided by the supplier is reported in Table 1. The depositions were carried out by means of a cold spray system (CGT-Kinetiks 3000; CGT Cold Gas Technology GmbH, Ampfing, Germany). A special polymeric nozzle designed for aluminium powder spraying was used. The coatings were deposited on different geometries of AA6061-O aluminium alloy substrates: plate (laminated $50 \times 500 \times 4 \text{ mm}^3$) for spray optimization and metallographic analysis, four-point strips (laminated $76 \times 19 \times 2 \text{ mm}^3$) to perform four-point bending testing, cylindrical samples (25 mm diameter, 7 mm thickness) to perform adhesion testing following the ASTM C633 standard, cylindrical samples (25 mm diameter) to perform cohesion testing following the tubular coating tensile (TCT) test and square plate ($25.4 \times 25.4 \times 4 \text{ mm}^3$) to measure residual stress by the modified layer removal method (MLRM). The surfaces of the samples were grit-blasted with angular corundum (16 mesh) to optimize the coating adhesion. The average surface roughness was $R_a = 14.65 \pm 6.63 \mu\text{m}$, as determined by measuring one representative sample (three measurements for each sample: left corner, centre and opposite-right corner) for all different geometry substrates using an Alpha-Step IQ profilometer (KLA-Tencor Corporation, 1 Technology Drive, Milpitas, CA 95035) and following the DIN EN ISO 3274:1998 and 4288:1988 standards.

2.1 Cold Spray Deposition

The main spray parameters were maintained constant for all deposition sets: The stagnation gas temperature was 350 $^{\circ}\text{C}$, and the nitrogen stagnation gas pressure was kept constant at 3.1 MPa. The distance between the nozzle and the substrate was 20 mm (Fig. 1a), and the nozzle scan spacing was 1 mm (Fig. 1b); the powder flow and carrier gas flow rate (Ref 11) were the same for all depositions. The cold spray gun followed a zig-zag pattern on the aluminium substrate, and each subsequent pass was a repetition of the first pass. In particular, for the four-point strips, the pattern was the equivalent of the layout reported in Fig. 1(b). For all different substrate geometries (plate, four-point, adhesion, cohesion and MLRM), seven sets of three samples (four for adhesion) were deposited. In the first four sets (1–4) the (desired) coating thickness was varied (to 0.5, 1.0, 1.5 and 2.0 mm) with single-pass deposition; in the next three sets (5–7) the coating thickness (2 mm) was kept constant and the number of passes was varied (to two, three and four). There was no time delay between subsequent passes during multi-layer coating. The desired thickness was obtained by varying the gun traverse speed; in the case of cohesion substrates, the rotation speed of the cylindrical samples was varied to obtain coating uniformity and thickness. The coating thickness reported for each set is the average of three gauge measurements for each sample of the set (for a total of nine measurements). The standard deviation is also reported. The process setup and coating thickness for the different samples are summarized in Tables 2 and 3.

2.2 Metallographic Sample Preparation

The coating microstructure (plate samples; see Table 3) was investigated by means of cross-sectional light optical microscopy (LOM, model DM6000M; Leica, Wetzlar, Germany). All samples were sectioned and mounted. Grinding was performed using different grades of abrasive papers with a final polish using 1- μm diamond suspension. Samples were also chemically etched using modified Keller's reagent (2.5 mL NHO_3 , 1.0 mL HCl , 1.5 mL HF , 95 mL water).

2.3 Image Analysis

The areal percentage porosity of the coating was measured by image analysis. LOM micrographs of the coating (plate samples; see Table 3) were processed by scanning probe image processing (SPIP; Image Metrology A/S, Hørsholm, Denmark) software set to detect and analyze grains, particles, inclusions and pores (according to ASTM 1382 standard) (Ref 13). Five LOM micrographs at 100 \times and five different LOM micrographs at 200 \times were processed for each set of samples. The coating–substrate interface porosity was not considered.

The same software, following ISO 13322:2004, was used to analyze LOM images (100 \times and 200 \times) of dispersed particles for the purpose of determining particle size distributions.

2.4 Microhardness Analysis

Microhardness measurements on metallographically prepared cross-sections (plate samples; see Table 3) were also performed. Using a microhardness tester (VMH-TAUTO; Leica, Wetzlar, Germany) starting at the coating surface and reaching the substrate using step size of 50 μm , Vickers indentations at 10 g load were performed within each coating. The average microhardness of the powder and its standard deviation are also reported; more than 20 indentations were performed on a metallographically prepared sample.

2.5 Adhesion and Cohesion Tests

Adhesion and cohesion tests were performed following ASTM C633 and the TCT test. A mechanical testing machine (MTS Systems Corporation, Eden Prairie, MN) under force control was used, and the load was measured using a 50-kN load cell (MTS Systems Corporation). The average and standard deviation of measurements per set of three cohesion samples (Table 3) and four adhesion samples (Table 3) were calculated.

2.6 Thermal Analysis

Thermal analysis was performed on adhesion samples during deposition using the parameters in Table 1. The adhesion samples were drilled at the centre of the back side with respect to the deposition surface, and a K-type thermocouple was positioned (embedded in the sample) at 0.5 mm from the deposition surface. Data were recorded using a Fluke 17B digital multimeter (Fluke Corporation,

6920 Seaway Blvd Everett, WA 98203, USA) at a frequency of one measurement per second. To reduce the influence of the different gun approach to the sample, data records were started at 60 °C for all measurements.

2.7 Residual Stress Measurements (MLRM)

The MLRM allows measurement of the dimensional deformation of a substrate after removal of subsequent layers by mechanical polishing. Automatic grinding (AbraPol-20 Struers Ltd., Mississauga, Canada) was performed using 30 grit abrasive paper for 15–20 s at 75 N at rotation speed of 150 rpm. The principle of this characterization is based on measurements of substrate displacements induced by removing a small layer of stressed coating. In this work, the related strains along the surface were measured using a strain gauge (Vishay CEA-125WT-120/350; Vishay Precision Group, Malvern, PA), recorded by means of a strain indicator (Vishay Micro-Measurements mod. P3) and converted via software into relative stresses according to Kroupa and Rybicki (Ref 14, 15). The strain gauge was glued at the centre of the uncoated side of a sample after cleaning the substrate surface with degreasing agents. Wires were welded onto the terminals and protected with a sealant to avoid exposure (to water, etc.). Measurements were performed with respect to two orthogonal directions of the MLRM sample (Table 3): longitudinal and transverse. The average of all the longitudinal and transverse depth profile measurements was taken to characterize the residual stress of the coating.

Table 1 Aluminium alloy 6061 powder composition

Element	wt. %
Silicon	0.63
Iron	0.42
Copper	0.22
Manganese	0.09
Magnesium	1.00
Chromium	0.31
Zinc	0.18
Titanium	0.09
Other	0.12
Aluminium	Remainder

Moreover, the variation of the average residual stress measurements inside subsequent layers of 0.6 mm thickness from the coating interface up to the coating surface was analyzed; no further consideration of depth profiles was considered because they were reported in a previous study (Ref 12).

2.8 Four-Point Bending Tests

All four-point bending tests were performed in a four-point bending rig under force control using an MTS mechanical testing machine (MTS Systems Corporation). The load was measured using a 50-kN load cell (MTS Systems Corporation). In the upper and lower load applicators, the convex (radius 0.003 m) knife edges were spaced 0.06 and 0.04 m apart, respectively. The tests were carried out under tensile load for the coating (four-point samples; see Table 3); i.e., the coating was positioned in contact with the more widely spaced knives. The bending strength, σ , was computed from the maximum load P_r that caused the coating to rupture using the standard relationship (ASTM E855/90)

$$\sigma_r = \frac{3P_r a}{bh^2}, \quad (\text{Eq 1})$$

where a is the spacing (normal to the load) between the upper and lower loading knives, and b and h are the specimen width and thickness, respectively.

The maximum (rupture) strain ε_r in the limit of small bending is given by

Table 2 Main deposition parameters

Spray parameter	Plate, four-point, adhesion, MLRM (samples)	Cohesion (sample)
Gas temp.	350 °C	350 °C
Gas press.	3.1 MPa	3.1 MPa
Stand-off dist.	20 mm	20 mm
Scan spacing	1 mm	1 mm (estimated)
Scan speed	24, 12, 8, 6 mm/s	0.4, 0.3, 0.2, 0.1 mm/s
Sample rotation	...	22, 18, 12, 6 rpm
No. of passes	1–4	1–4

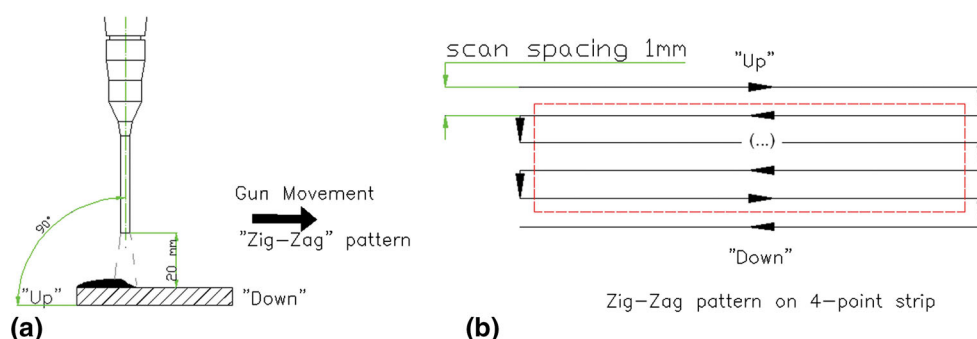









Fig. 1 (a) Nozzle–substrate relative angle and stand-off distance. (b) Zig-zag pattern of deposition on substrate (in particular: four-point strip)

Table 3 Coating thickness (mm) of the entire set of samples obtained by cold spray deposition of AA6061 powder on AA6061 substrates

Sample	Set 1 	Set 2 	Set 3 	Set 4 	Set 5 	Set 6 	Set 7 
Plate	0.50 ± 0.06	1.04 ± 0.11	1.51 ± 0.09	1.87 ± 0.07	2.01 ± 0.15	2.12 ± 0.15	2.05 ± 0.16
Four-point	0.58 ± 0.05	1.19 ± 0.04	1.80 ± 0.08	2.47 ± 0.01	2.40 ± 0.08	2.51 ± 0.01	2.49 ± 0.05
Adhesion	0.64 ± 0.06	1.26 ± 0.05	1.77 ± 0.05	2.48 ± 0.05	2.50 ± 0.09	2.46 ± 0.12	2.52 ± 0.14
Cohesion	0.60 ± 0.03	0.79 ± 0.02	1.15 ± 0.01	2.11 ± 0.10	2.13 ± 0.01	2.15 ± 0.04	2.06 ± 0.03
MLRM	0.65 ± 0.18	1.24 ± 0.10	1.73 ± 0.08	2.15 ± 0.09	2.32 ± 0.20	2.55 ± 0.10	2.56 ± 0.08

$$\varepsilon_r = \frac{h\Delta z}{a(L - 2a)}, \quad (\text{Eq } 2)$$

where Δz is the linear (rupture) displacement of the load applicator in the direction of load and L is the larger spacing of the upper knives. The elastic modulus was computed from Eq 1 and 2 using Hooke's law. Uncoated strips (of 2 and 4 mm thickness) were also tested. In these cases, where there was no breakage, and also for set 1, where it was difficult to identify the coating breakage point, the load P_r (to calculate the bending strength) and the displacement Δz (to calculate the strain) were taken from the load–displacement curve in the upper limit of linearity (elastic behaviour). This upper limit of linearity was calculated by the instrument software by considering the second derivative of the load–displacement curve.

2.9 Fractographic Analysis

To properly interpret the mechanical testing results and the four-point test measurements and to determine the failure dynamics, the characteristics of the fracture surfaces of the cohesion samples after testing were qualitatively analyzed by scanning electron microscopy (SEM, model VEGA LMU; TESCAN, Brno, Czech Republic).

3. Results and Discussion

A preliminary consideration is necessary because there are differences in thickness for the different substrates (plate, four-point and adhesion) obtained by the same cold spray deposition process (Tables 2, 3). This discrepancy, already noted in a previous work (Ref 12), is mainly due to the different substrate geometry and heat capacity of the sample holder, which affects the sample temperature during spraying. Higher substrate temperature enhances the deposition efficiency, as reported by Kulmala and Vuoristo (Ref 16).

3.1 Microstructure and Pore Analysis

The particles are spherical with the presence of some satellites, as indicated by arrows in the SEM micrograph of Fig. 2(a). The particle distributions shown in Fig. 2(b), as determined from LOM images, agree with the powder datasheet provided by the manufacturer. The particle

distribution count shows a bimodal trend with two main peaks at 9 and 22 μm . The gas-atomized particles show a grain microstructure in Fig. 3(a). Aluminium coatings show compact microstructure with the presence of porosity, as shown in Fig. 3(b) and 4. The pores are mainly elongated and interstitial, as shown in Fig. 3(b). In all etched coatings, the microstructure showed no noticeable variation as a function of thickness or the number of layers in the range investigated; the grain particle microstructure was preserved in the coatings, and no recrystallization or grain refinement was noticed. At the substrate–coating interface, the presence of alumina particles used for grit blasting can be seen in all the samples in Fig. 4. Porosity analyses were performed on all coating sets (Fig. 4), and the results are reported in Fig. 5. The average and standard deviation of the porosity showed different trends: the former as a function of coating thickness (1–4), and the latter as a function of the number of passes (4–7). The porosity ranged between 0.3 and 1.1% of coating area, and was constant (at about 0.3%) within the statistical error for the set obtained using a single pass with varying coating thickness. Sets 4–7, with increasing number of passes but constant coating thickness, exhibited increasing porosity as a function of the number of passes, in agreement with a previous work (Ref 12) where a localized increase in porosity was observed between two subsequent passes.

3.2 Mechanical Properties

3.2.1 Microhardness Analysis. The Vickers indentation profiles indicated that the microhardness was mainly constant through the coating thickness, so the mean coating microhardness was used in computing the average of the entire dataset. The results are shown in Fig. 6, where the average Vickers hardness of the aluminium alloy coatings is reported for each set. The coatings exhibited average microhardness of about 100 HV0.01. In comparison, the microhardness of the particles was 64 ± 8 HV0.01, indicating that the particles were hardened during deposition, as reported in other works (Ref 11, 17, 18). The maximum average microhardness (105 HV0.01) was obtained for set 4 (1.9 mm thick, single pass).

3.2.2 Influence of Hot Gas Flux on Residual Stress Measurements. The MLRM trend (Fig. 7a) shows a decrease in the absolute residual stress from 100 MPa to

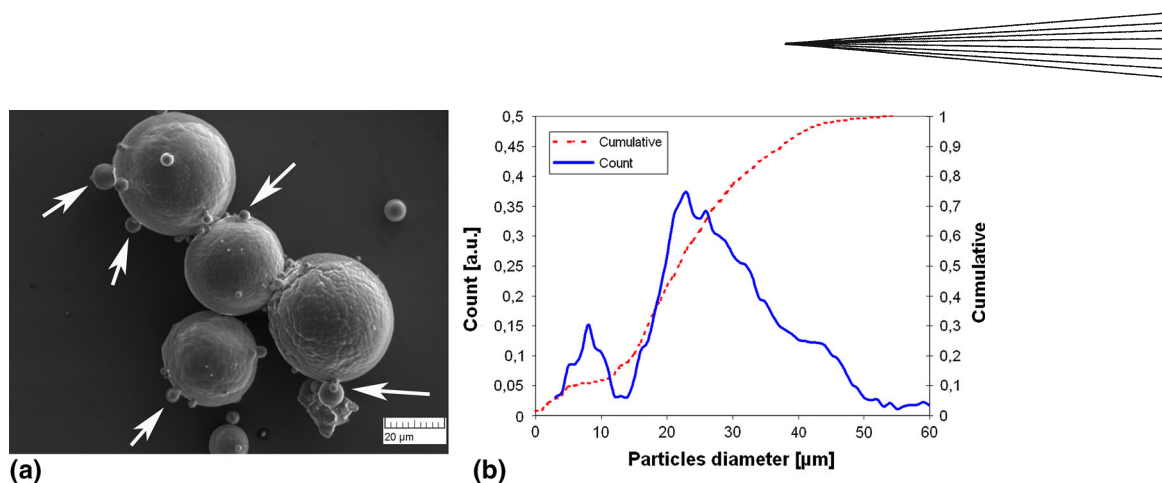


Fig. 2 (a) SEM micrographs of AA6061 aluminium alloy powder: spherical particles with the presence of satellites (indicated by arrows). (b) Distribution of particle diameter of AA6061 powder

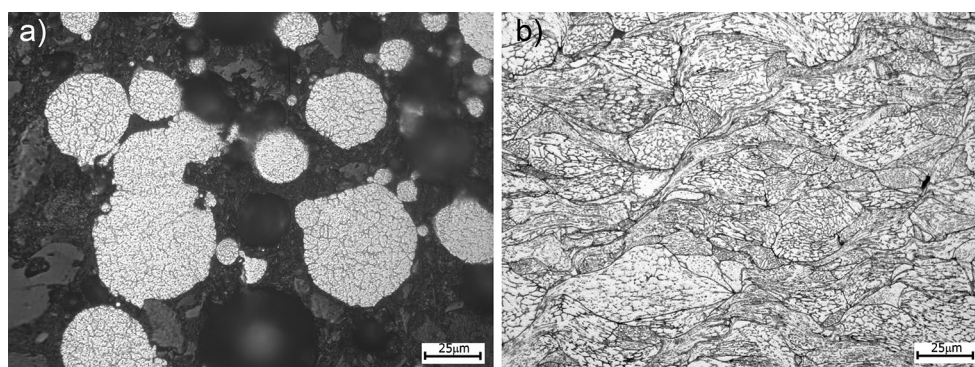


Fig. 3 LOM micrographs of AA6061 aluminium alloy powder and AA6061 coating (set 6) etched by modified Keller's reagent. (a) Gas atomized powder. (b) Microstructure of coating

about 60 MPa with increasing coating thickness in sets 1–4. The multi-pass coatings (sets 5–7) and the thickest single-pass coating (set 4) exhibited compressive residual stresses of about 60 MPa. This behaviour is compatible with a stress-relief behaviour that is a function of the heated substrate temperature during deposition due to the permanence time of the hot process gas (bow shock) on the substrate (Ref 19), as reported previously (Ref 12). To confirm such stress relief, the stress behaviour near the coating–substrate interface and at the coating surface was analyzed. The average stress measurements inside subsequent layers of 0.6 mm thickness from the coating interface up to the coating surface are shown in Fig. 7(c). The compressive residual stress near the interface decreases to 30 MPa with increasing coating thickness, independently of the number of passes; in contrast, the residual stress in the coating surface remains constant (at about 90 MPa for all sets), as shown in Fig. 7(d). The coating interface, with respect to the coating surface, had a prolonged exposure time to the cold-spray hot gas flux (Ref 19), giving rise to greater stress relief. To confirm this hypothesis, the temperature during spray deposition was measured. The location of the thermocouple inside the sample, the zig-zag pattern of deposition and the sample temperature, measured as a function of deposition time, are reported in Fig. 8. For the single-pass coatings (sets 1–4),

the exposure time to temperature greater than 60 °C (up to a maximum of about 190 °C) was 165, 170, 295 and 480 s, respectively, while for the multi-pass coatings (sets 5–7), this exposure time was the same at about 490 s. Other considerations relating to temperature based on analysis of the time–temperature curves in Fig. 8 must also be reported. The gun movement following a zig-zag pattern induced a double fluctuation of temperature at each point of the sample. The first, rapid, variation is due to the hot gas flux that runs across and outside the sample during each scan (Fig. 8b), raising and lowering the temperature. The second fluctuation of temperature, present only for multi-pass deposition, is due to the repetition of the whole zig-zag pattern. Taking into account these two variations, the average temperature was calculated as the sum of the temperature measurements over 60 °C divided by the number of measurements (one per second); the values and standard deviations are reported in the time–temperature graph in Fig. 8. Heat treatment for stress relief to reduce distortion or high stress of AA6061 alloy is performed at 160 °C, as reported in Ref 20. This temperature is compatible with the sample temperature measured during the spray deposition. It is well known that stress relief is a time–temperature-related phenomenon (Ref 20), so considering the reported exposure time and the graph in Fig. 7(d), there is evidence of stress relief of the coating

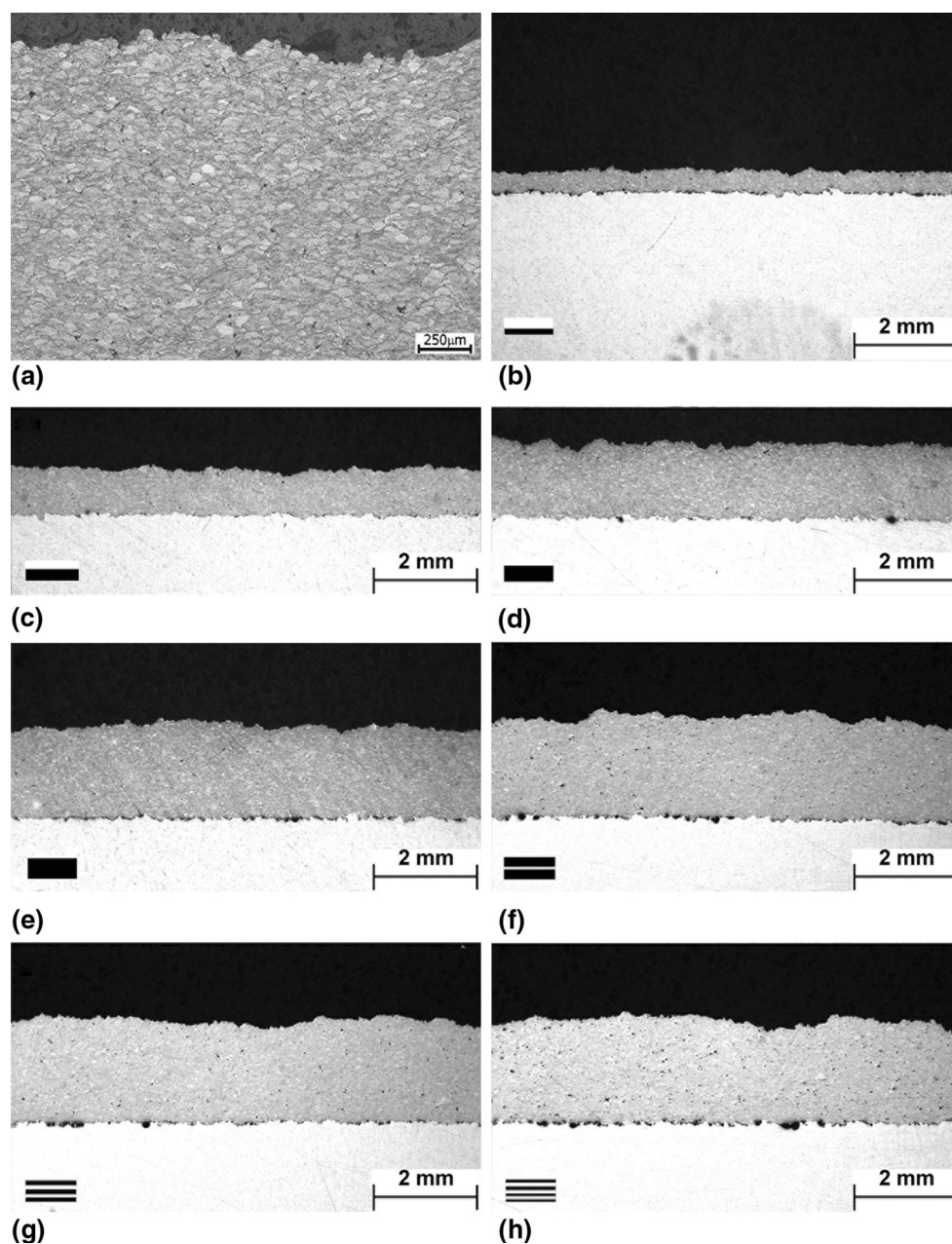


Fig. 4 LOM micrographs of AA6061 coatings etched by modified Keller's reagent. (a) Compact microstructure of coating (set 6). (b–e) Single-pass coatings of different thickness (set 1, 2, 3 and 4, respectively). (f–h) Multi-pass coatings (set 5, 6 and 7, respectively)

near the substrate interface as a function of deposition time.

3.2.3 Influence of Residual Stress on Coating Adhesion. All the tested adhesion samples exhibited adhesion failure at the substrate–coating interface; no cohesion failure was observed. Similar to previous observations, there were distinct trends for the single-pass and multi-pass coatings (Fig. 9). In the range examined for the single-pass coatings, the adhesion to the substrate appeared not to be affected by the coating thickness and the adhesion strength was constant at 33 MPa. Increasing the number of passes negatively affected the coating adhesion.

The single-pass coating with 2.5 mm thickness exhibited adhesion strength of 31 MPa, while this dropped to 21 MPa for the four-pass coating with 2.5 mm thickness. Although there may be a correlation between the stress relief at the coating interface and particle–substrate interlocking, relating the stress measurements (Fig. 7) to the adhesion results (Fig. 9), it is clear there are other causes affecting the adhesion that directly involve the increase of the number of layers. In fact, stress relief at the interface could loosen the mechanical adhesion between the particles interlocked with the substrate; however, the stress behaviour was shown to be correlated with the

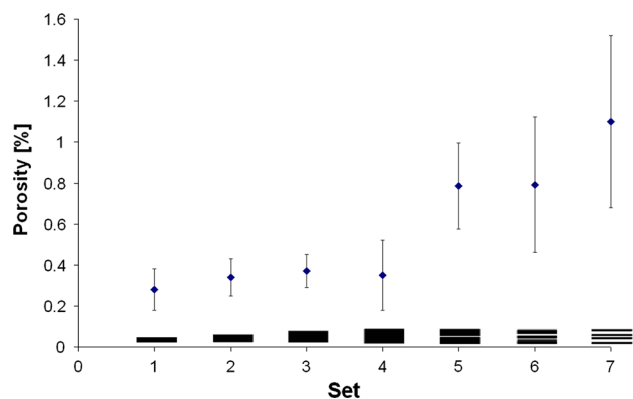


Fig. 5 Average and standard deviation of coating porosity obtained by image analysis

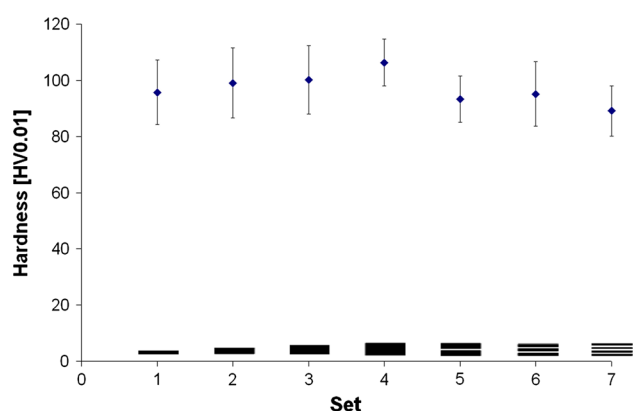


Fig. 6 Average coating microhardness obtained by depth profile measurements and its standard deviation. The microhardness of the powder was 64 ± 8 HV0.01

coating thickness, not the numbers of layers, as found in the adhesion results. Another result coming from stress analysis, reported in a previous study (Ref 12), highlighted the presence of tensile peaks (150 MPa) at the interfaces between layers. Although the mechanism that negatively affects the adhesion as the number of passes increases is not yet understood, the presence of such tensile peaks in the coating could play a role in the coating adhesion failure. More targeted investigations are ongoing.

3.2.4 Evaluation of Deposition Strategies by Tensile (TCT) and Bending (Four-Point) Tests. The results of the cohesion (TCT) analysis were quite different from previous observations; there was no evidence of any particular trends as a function of thickness nor as a function of the number of passes, as can be seen in Fig. 9. Only set 1, with thickness of 0.6 mm, exhibited slightly higher cohesion strength than the other sets. Ultimately, the cohesive strength for all the sets was relatively constant at about 80 MPa for all thicknesses and numbers of layers. The multilayer deposition strategy did not affect the cohesion results; in this case, the tensile load of the cohesion test acted parallel (shear force) to the subsequent layer interfaces without any appreciable influence on coating cohesion. To evaluate and understand the behaviour of

the mechanical properties, the ultimate (rupture) strength and modulus when the tensile load was applied perpendicular to the interface layers were measured using a four-point bending test performed according to the geometrical deposition parameters (zig-zag pattern, parallel to the long axis of the four-point sample of Fig. 1b).

The load–extension chart in Fig. 10 presents representative measurements obtained from the four-point bending tests evaluating the seven sets and the blank substrates (with thickness of 2 and 4 mm). The blank AA6061-O samples exhibited elastic and plastic behaviour. The samples of set 1 also showed elastic and plastic behaviour; although there were several cracks in the coating (Fig. 10c), there was no appreciable indication of their influence on the load or extension measurements. Set 2, for load greater than 1 kN, exhibited two successive breaks: the first at extension of 0.6 mm, and the second at 0.8 mm. The two transverse cracks on the coatings appeared at the loads applied by the knives. The measurements proceeded after the breaks without an increase in load until the extension reached 2 mm, at which point the coating delaminated from the substrate. All the cracks reported were transverse, i.e. parallel to the sample width (Fig. 10c) and, referring to Fig. 1(b), perpendicular to the gun movement during spraying. The pattern of deposition, in particular the spray direction, has a great influence on the bending tests. The pattern of Fig. 1(b) was selected to avoid the possibility of transverse crack propagation through the coating parallel to the deposition scan direction. Test results showed that deposition with the spray direction parallel to the four-point strip dramatically reduced the rupture load P_r . As an example, the rupture load of the 2-mm single-pass coating was 17 MPa, 55% lower than for the corresponding sample deposited with the spray direction perpendicular to the strip.

After complete detachment of the coating between the two cracks, the load–extension curve advanced following the same plastic trend as for the blank samples. The other sets (3–7) showed the same load–extension trend as described for set 2, but the first break was much more evident and easy to identify in the curve. In the load–extension chart (Fig. 10a) for sets 3–7, data are reported up to the second break; a magnification of these curves (up to the first crack) is reported in Fig. 10(b).

The elastic modulus of samples of the seven sets and blank strips was also calculated using Eq 1 and 2. The results (average and standard deviation) and the relative loads at breakage (average and standard deviation) are reported in the histogram in Fig. 11. The load at breakage, as expected, increased as the coating thickness was increased (sets 1–4). Considering the sets comparing different numbers of layers (sets 4–7 with equal thickness), a large difference is noticeable between the single- and multi-layer coatings; the coatings deposited in two, three and four passes showed similar loads at breakage (2.4–2.5 kN), being 14–19% higher than the load at breakage (2.1 kN) reported for the single-pass coating.

The bending elastic modulus (Fig. 11) calculated for the blank AA6061-O laminated strips was 96.6 ± 3.3 and 91.5 ± 0.3 GPa for 2 and 4 mm strips, respectively, higher

than the well-known modulus measured in tension of 60–70 GPa (Ref 20). This discrepancy between measurements in (three- or four-point) bending versus tension is well known, as reported by Berthelot and Fatmi (Ref 21). The modulus value, which was maximum for the blank samples, decreased for sets 1–4 with increasing deposition thickness (on substrates of the same thickness). The elastic modulus increased for each added layer as a function of the number of layers (sets 4–7).

A four-point bending test performed on a strip with a coating measures the mechanical properties of the whole sample (strip plus coating), and such measurements are quite helpful to understand the interaction of the coating with the bulk material. However, it is also important to understand the mechanical behaviour of the coating without the influence of the strip. The modulus of the freestanding coating (without the strip) can be evaluated by linear regression considering the behaviour of the elastic modulus of the samples as the coating thickness increases with respect to the constant thickness of the strip, i.e. in sets 1–4. Some considerations are necessary for this analysis. The four-point bending test acts on samples

Fig. 8 Thermal analysis of cold spray deposition on adhesion substrates. (a) Position of the thermocouple inside the sample. (b) Zig-zag pattern of deposition. Time-temperature graphs for (c) single-pass set 1, (d) single-pass set 2, (e) single-pass set 3, (f) single-pass set 4, (g) two-pass set 5, (h) three-pass set 6, (i) four-pass set 7. Each graph shows the sum of the temperatures $> 60^\circ\text{C}$ divided by the exposure time

(with or without coating) by applying both tensile and compressive load. The tensile load is applied on the top side of the sample (upper knives), while the compressive load is applied on the bottom side of the sample (lower knives). Based on this consideration, the coatings of sets 1–3 in the bending test were subjected only to tensile load, while the thicker coatings of sets 4–7 were loaded principally under tension; however, there was a compressive load in the thin layer from the coating–substrate interface up to the middle of the sample thickness (strip plus coating), as indicated in the upper-left layout in Fig. 12(a). In the same manner, the 2-mm strips, the substrate of all the coatings, were subjected to tensile and compressive load for sets 1–3 but only compressive load

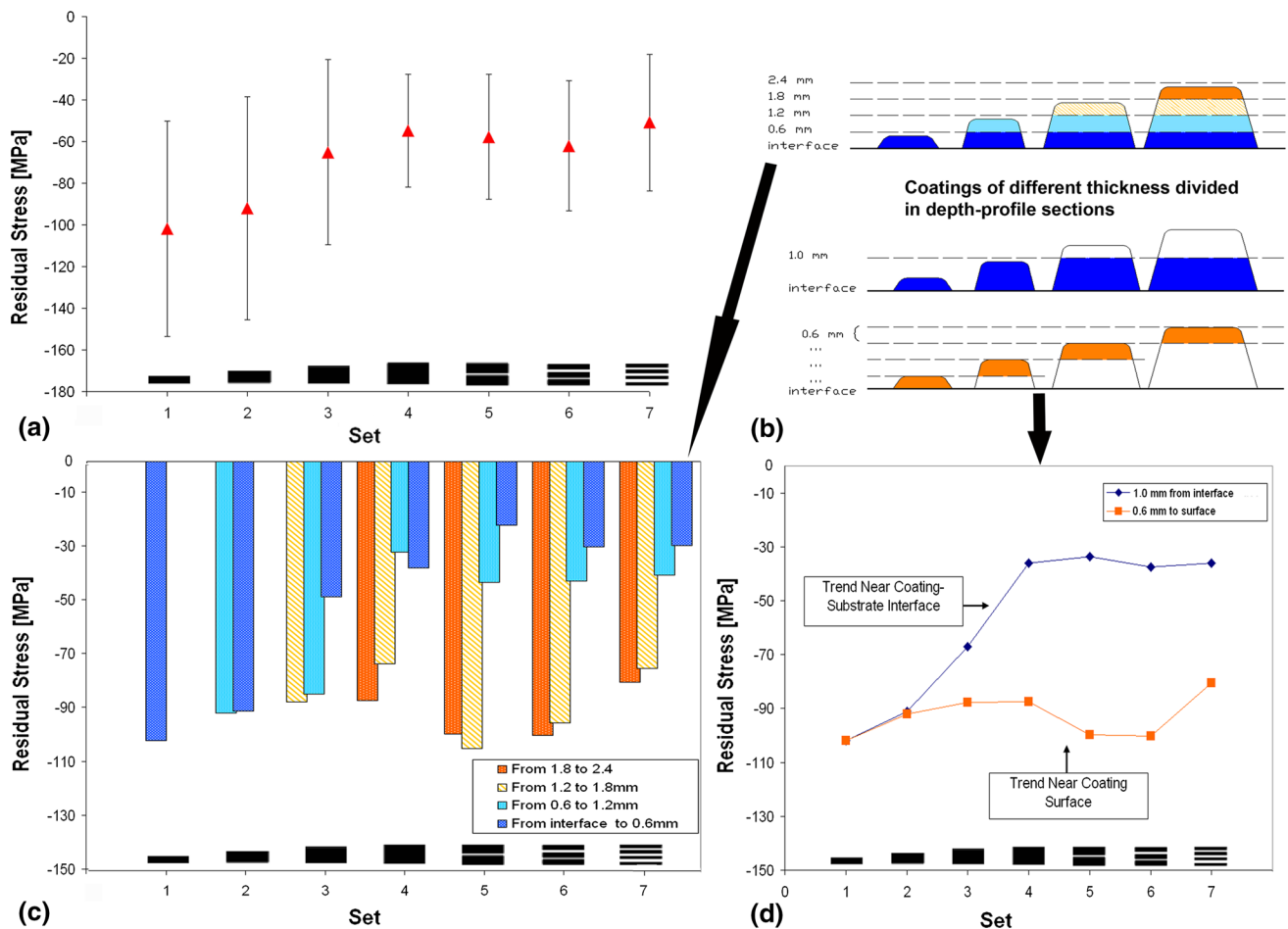
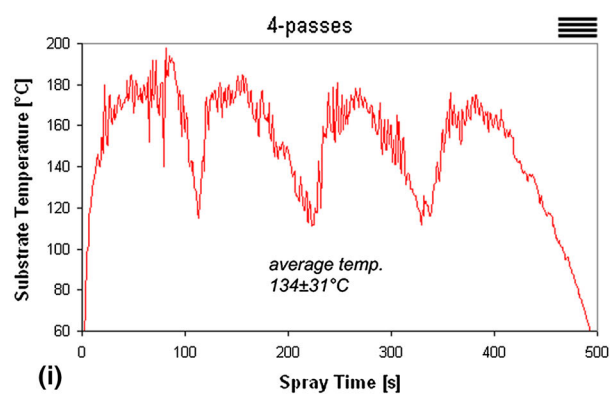
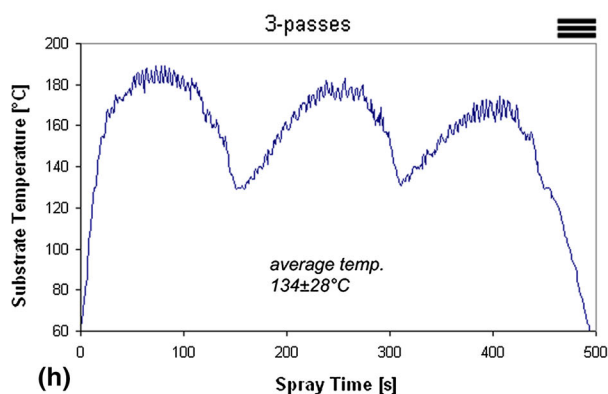
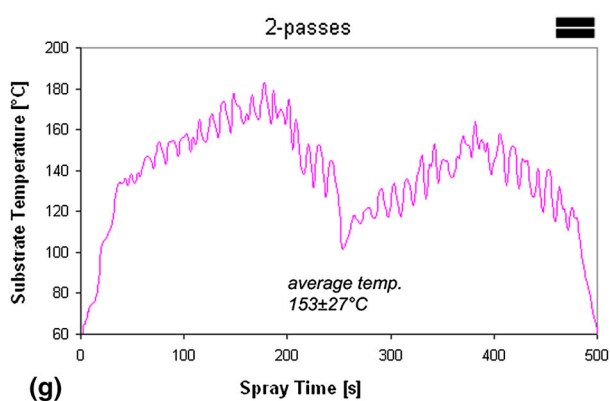
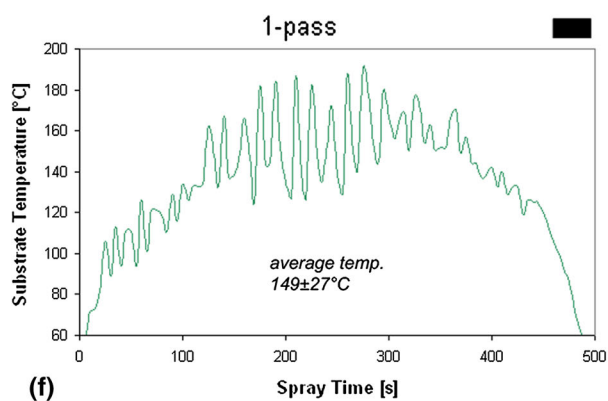
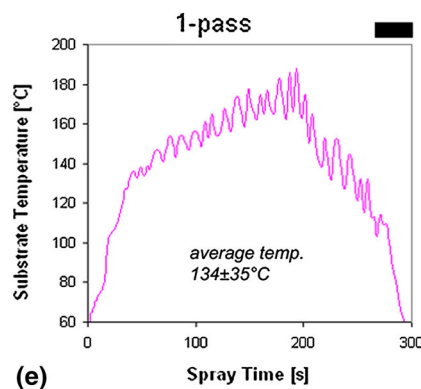
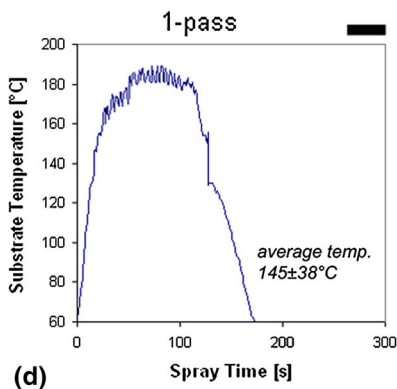
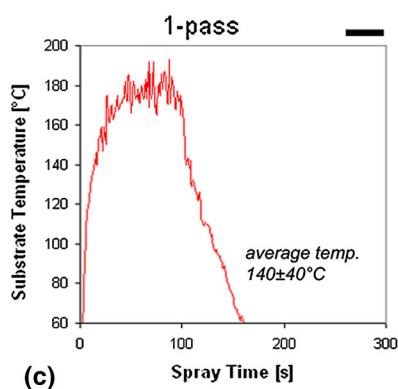
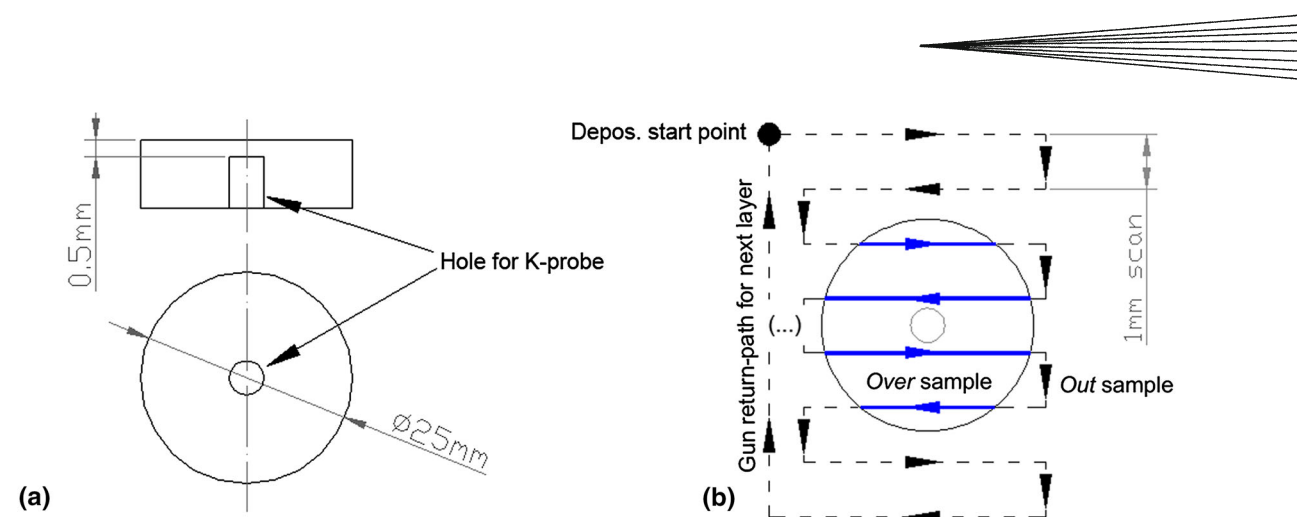


Fig. 7 Residual stresses obtained by depth profile measurements performed by MLRM. (a) Average coating residual stress. (b) Layouts of the coatings divided into sections for depth-profile stress analysis. (c) Average residual stress measured inside subsequent layers of 0.6 mm thickness from the coating interface up to the coating surface. (d) Average residual stress measured near the interface and at the coating surface



for the samples of sets 4–7. Another consideration that must be taken into account for bulk material is that compressive and tensile tests give the same Young's modulus; only the presence of defects such as porosity or voids can reduce the results measured in a tensile with respect to a compressive test, because pores and voids may open easily under tensile loading. This is not the case for AA6061 coatings. In fact, examining the increase of porosity reported for the multilayer coatings in Fig. 5 and comparing the results with the modulus reported in the histogram of Fig. 11, an increase in the modulus is observed as the number of layers grows.

All these considerations validate the approach of using linear regression to evaluate the elastic modulus of free-standing coatings. In Fig. 12(a), the elastic modulus as a function of the ratio of the strip and coating section (A) to the coating section (A_c) shows that the elastic modulus is linearly dependent on this ratio (with a quadratic correlation coefficient of 0.9985). In the linear regression, the influence of the substrate decreases with increasing coating thickness, and when the ratio A/A_c is equal to 1, the thickness of the coating is equal to the thickness of the

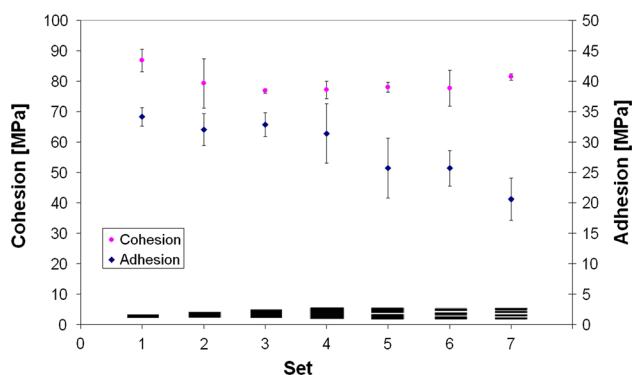
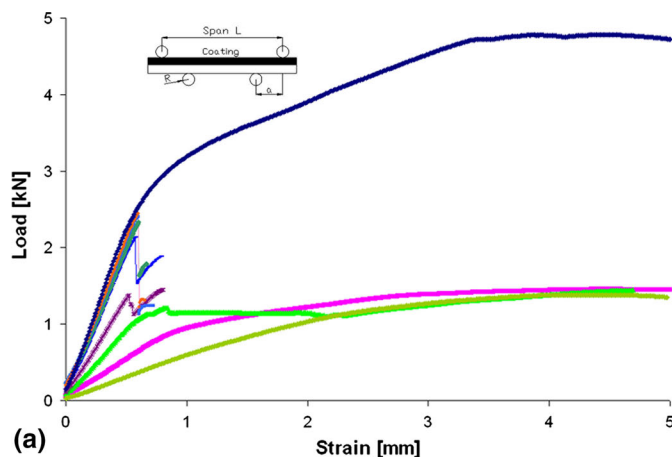


Fig. 9 Adhesion and cohesion measurements following standard ASTM C633 and TCT test



whole sample and the strip thickness is equal to zero. In this case ($\lim A/A_c = 1$ for $A_c \rightarrow A$) the elastic modulus of 38 MPa reported in Fig. 12(a) is the elastic modulus of the freestanding single-pass coatings of sets 1–4. Conversely, the influence of the substrate can be easily determined by subtracting the obtained elastic modulus of the freestanding (single-pass) coating from the elastic modulus of each sample (coating plus strip) for each set of the linear regression.

Noting that the modulus of the multi-pass coatings of sets 4–7 grows with increasing number of layers, as shown in Fig. 11, and that all these sets (4–7) have the same thickness, it is easy to estimate the elastic modulus of the freestanding coatings of the multi-pass set by removing the influence of the substrate as derived from the linear regression (set 4) of the single-pass coatings. The free-standing modulus of the multi-pass coatings is presented in Fig. 12(b), where the percentage of the modulus with

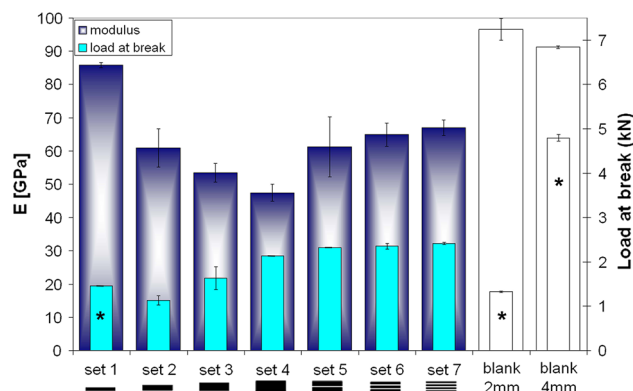


Fig. 11 Histogram of average load at breakage and the calculated elastic modulus. The errors reported are standard deviations. Asterisk indicates the breakage point (also displacement point), taken as the upper limit of linearity (elastic behaviour) of the load–displacement data

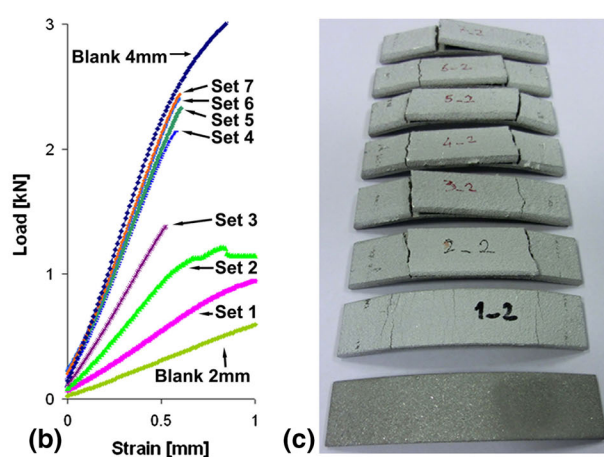


Fig. 10 (a) Load–extension chart, reporting the first and second coating crack. (b) Load–extension chart (magnification), showing only the first crack. (c) Samples after the four-point test. The apparatus was configured as in the schematic (top right); $L = 60$ mm, $a = 10$ mm, $R = 3$ mm

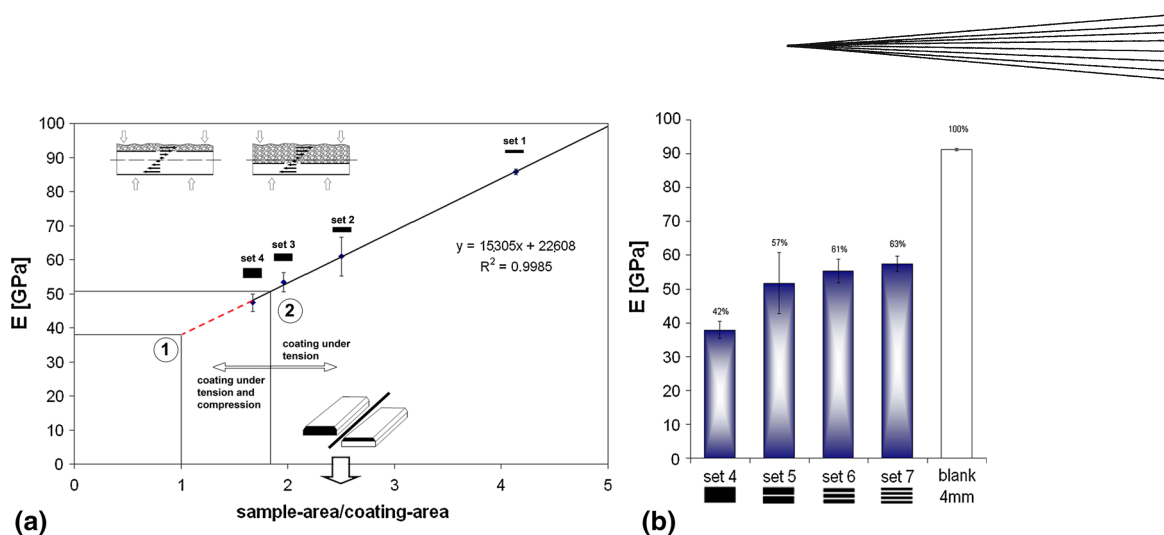


Fig. 12 (a) Linear regression of elastic modulus as a function of the strip+coating:coating section ratio. Point (1) evaluation of freestanding coating modulus. Point (2) limit between coating work-load under tension and under tension and compression. (b) Elastic modulus calculated by regression of freestanding coatings compared with elastic modulus of 4-mm strip (blank sample)

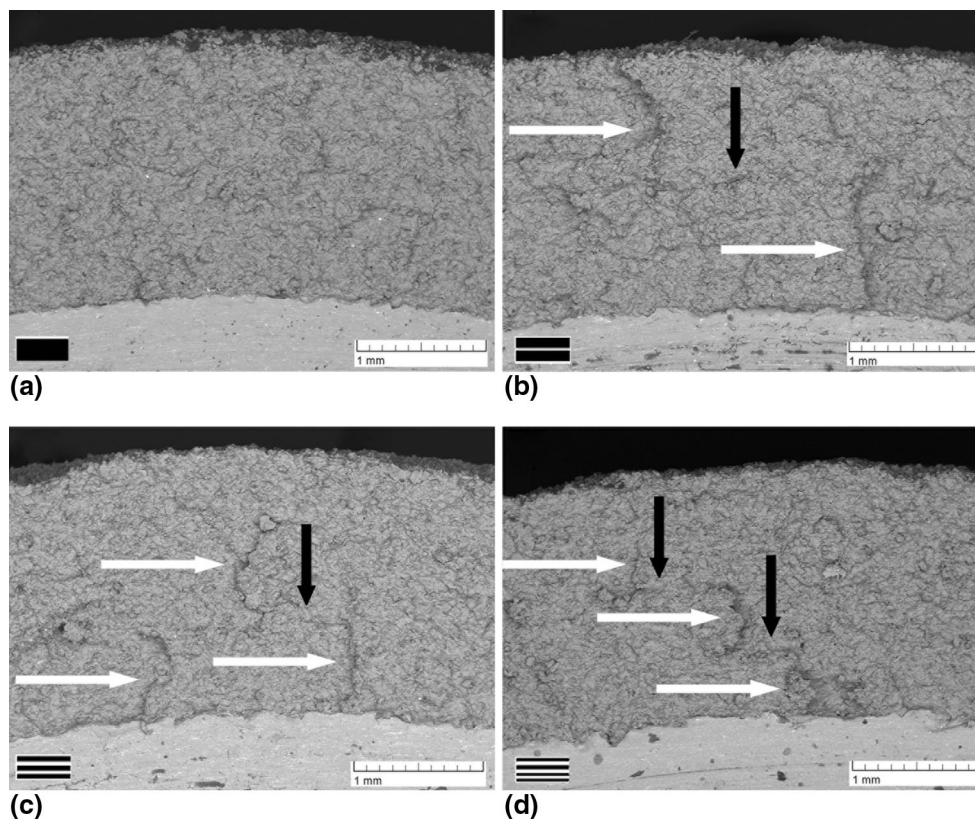


Fig. 13 SEM micrographs of AA6061 coating fractures. (a) Homogeneous fracture. (b–d) Evidence of interlayer cracks (black arrows) and crack propagation between layers (white arrows)

respect to bulk material (4-mm blank sample) is also reported. Evaluation of the single-pass coating with respect to the multi-pass coating and bulk material (Fig. 12b) shows that the elastic modulus of the cold-sprayed free-standing coatings increased from 38 GPa (sets 1–4) up to 58 GPa (four layers, set 7), being 63% lower in comparison with the value of 92 GPa for the 4-mm blank sample. This behaviour of the modulus can be further understood

by analyzing the different mechanism of fracture of each coating.

3.3 Failure Analysis

The fractures analyzed for the deposits of sets 1–4 (single pass, different thicknesses) did not reveal any differences; the fractures were homogeneous, as presented in

the representative micrograph in Fig. 13(a). The coatings of set 5 (two-pass coating) showed a fracture with the presence of two crack typologies: one perpendicular to the substrate (indicated by white arrows in Fig. 13b), and the other parallel to the substrate (indicated by black arrows).

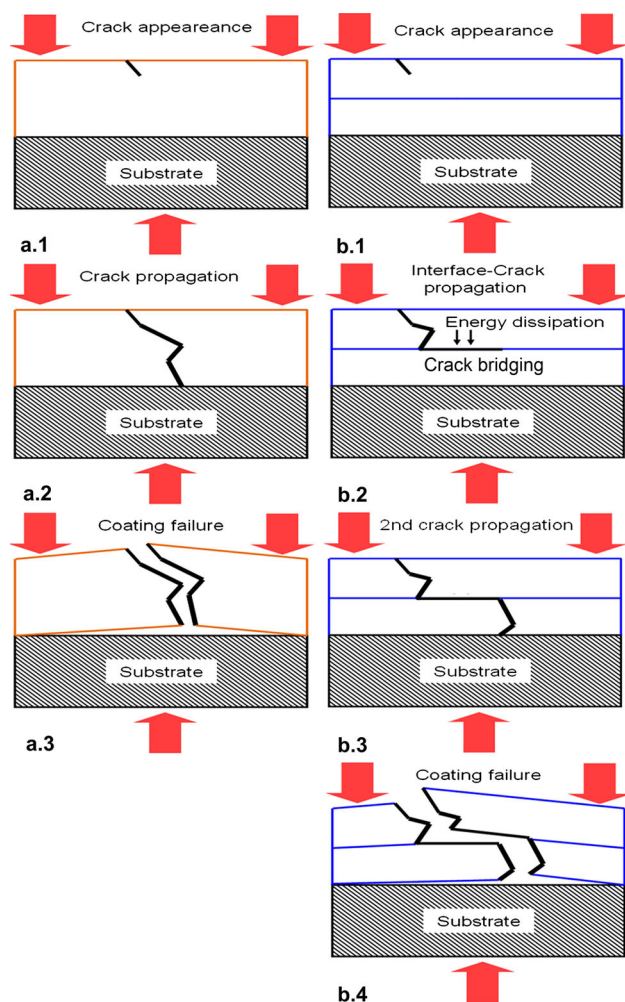


Fig. 14 (a) Schematic single-pass coating failure. (b) Schematic multi-pass coating failure

The perpendicular cracks propagated (geometrically) from the coating surface to the substrate, stopping at the middle of the deposit, close to the interface of the two adjacent layers. From there, the second parallel cracks started and continued until intersecting new perpendicular cracks which, from this point, propagated to the substrate. Similar behaviour was noticed in other multilayer deposits (Fig. 13c, d), where the perpendicular cracks come from the surface or layer interface to the adjacent layer interface (or substrate), while the parallel cracks follow the layer interfaces. This failure analysis shows that, after initiation, a crack propagates until it encounters a discontinuity in the coating such as the interface with the next layer. In some cases, the interface stops the crack propagation (e.g. in Fig. 13c, d), whereas in other cases, the crack continues along the interface (crack bridging). In both cases, additional energy is required to stretch the bridging along the interface, as reported by Evans and McMeeking (Ref 22) and Watanabe et al. (Ref 23). These failure mechanisms are represented in the schematic of Fig. 14, differentiating between the single-pass coating (Fig. 14a) and multi-pass coating (Fig. 14b).

When examined at higher magnifications, the surfaces mainly showed brittle interparticle fracture (Fig. 15a), although ductile fracture was observed in highly deformed particles in dimples, as shown in Fig. 15(b).

4. Conclusions

AA6061 aluminium alloy powder was deposited by cold spraying on AA6061-O substrate to perform metallographic, mechanical and fractographic analyses. Seven coating sets were produced for each type of characterization. For sets 1–4, the coating was deposited in a single pass with varying coating thickness, whereas for sets 5–7 the coating was applied using multiple passes to achieve a constant overall coating thickness.

Metallographic examination of coating cross-sections using image analysis showed very low pore content (0.3%) in the single-pass coatings with a slight increase in porosity (up to 1.1%) as the number of coating layers was increased. It was observed that the increased porosity was

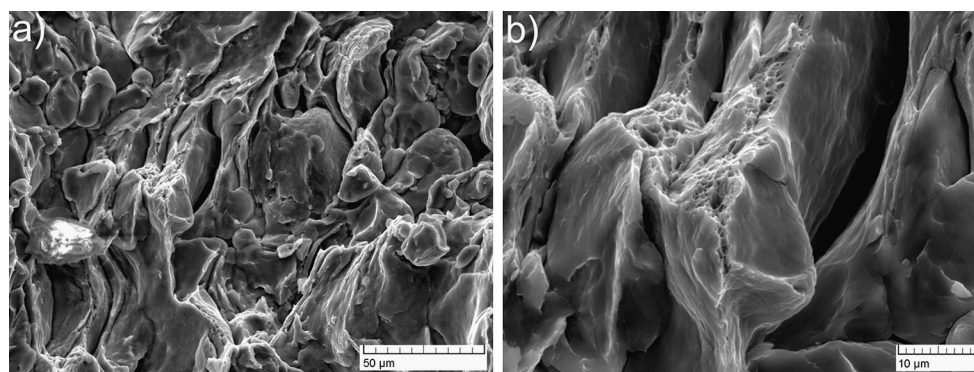


Fig. 15 (a) Interparticle brittle fractures and (b) dimpled appearance of ductile particle fracture

Table 4 Trends in mechanical properties of the coating as a function of thickness and number of passes

Property tested	Increasing thickness (single layer)	Increasing number of passes (multi-layers)
Porosity (image analysis)	→ 0.3%, stable	↑ < 1.1%, grows with number of layers
Vickers microhardness	→ ~100 HV0.01, stable	→ ~100 HV0.01, stable
Compressive stress (MLRM)	↓ (Intensity) [100 to 60 MPa], decreases with coating thickness	→ (Intensity) ~60 MPa, stable
Cohesion (TCT)	→ ~80 MPa, stable	→ ~80 MPa, stable
Adhesion (ASTM C633)	→ ~33 MPa, stable	↓ [31 to 21 MPa], decreases with number of layers
Four-point bending	→ Elastic modulus of freestanding coating stable	↑ Load at breakage and elastic modulus grow with number of layers

localized between two subsequent passes of the multilayer coatings.

The depth profile of microhardness showed a hardening (by about 50%) of the coating with respect to the gas-atomized particles. This behaviour can be attributed to an increase of the peening effect, densification and work-hardening of the coating (Ref 18). No particular trends outside the standard deviation were observed.

Measurements of the average compressive residual stress performed by stress depth profile analysis using the MLRM were stable at -60 MPa for the thicker coatings, independent of the number of passes used, while the absolute compressive stress was greater (up to -90 MPa) for lower coating thickness. From the depth profile analysis it was observed that, at the coating surface (from the surface to 0.6 mm from the surface) the stress was about -90 MPa for each set, while near the substrate-coating interface (from the interface up to 1 mm from the interface) the compressive stress intensity decreased with increasing coating thickness, independent of the number of passes (being about -30 MPa for sets 4–7). This behaviour is mainly attributed to thermal stress relief in proportion to the exposure time to the hot gas flux during deposition.

Mechanical study of the coatings based on TCT tests revealed that the cohesive strength was approximately 80 MPa for all sets. The tensile traction applied in the cohesion test acted parallel (shear force) to subsequent interfaces between layers of the coated cylindrical samples without any appreciable influence on the coating cohesion, so the multilayer deposition strategy did not affect the cohesion results.

The adhesion test results (following the ASTM C633 standard) revealed two trends, highlighted by the metallographic (pore) analysis: A constant value (more than 30 MPa) was observed for the single-layer coatings independent of the coating thickness, whereas a decrease in adhesive strength (from 31 MPa to 21 MPa) was observed as a function of the number of passes.

The four-point bending test results showed a reduction in the elastic modulus with increasing thickness of the coating deposited in a single pass on 2-mm-thick strips. Linear regression analysis of these samples showed that, for freestanding (without substrate) cold-sprayed single-pass coatings, the elastic modulus was 38 GPa, being 42% lower with respect to the modulus of AA6061-O laminated strip (92 GPa). Based on the same linear regression analysis and quite interestingly, an increase of the modu-

lus was observed for each added layer in the multi-pass (freestanding) coatings, being up to 58 GPa for the four-pass coating, i.e. 63% lower with respect to the blank sample. This behaviour is similar to that of laminate composites (Ref 24) and can be explained based on the fractographic analysis, where crack stopping and energy dissipation are localized at the interface with the next layer. All the data are summarized in Table 4.

The AA6061 cold-sprayed coatings deposited using the two different deposition strategies (single and multi-layers) showed different mechanical properties in the range of the presented investigation. The single-layer coating was more compact with less porosity. The multilayer coatings did not present uniformity through the coating section, the discontinuity between layers being highlighted by an intensification of the porosity at the interfaces. Not only are there morphological differences, but also variations in the mechanical properties at the interfaces between layers. In fact, in a previous study (Ref 12), tensile residual peaks localized between two subsequent layers were observed. These discontinuities do not influence the cohesion of the coating as measured by TCT, because the tensile load applied during this test acts parallel to the interfaces between layers in the coated cylindrical samples. Moreover, the discontinuity of the multi-layer properties, as for laminate composites, increases the elastic modulus as a function of the number of layers when tested by the four-point method. Indeed, in this test, the load is applied perpendicular to the layers.

The multi-pass strategy has the most negative effect on the coating adhesion. However, it has been hypothesized that there is a correlation with the tensile stress peaks at the interfaces between layers, although no direct relation was observed.

Finally, depth profile analysis of the residual stress revealed an area of stress relief near the coating-substrate interface. The residual stress value in this area decreases with increasing coating thickness, independent of the number of passes. This was attributed to the duration of hot gas flux during cold spraying of the sample.

This study highlights the importance of the choice of the cold spraying deposition strategy for the final properties of the coating, specifically that the geometrical deposition parameters play a role in the coating quality as a function of the type of stress to which the restored component will be subjected or its desired function. In most cases of damaged component repair, for example in the aeronautical industry, coating adhesion is a key

parameter, but not only high (standard) adhesion is required. Also, the value must be independent of the type of damage reconstruction; in particular, thicker, millimetric reconstruction must exhibit substrate adhesion like that of thin, sub-millimetric coatings. The constant adhesion value of single-pass deposition with respect to coating thickness (in the investigated range) and its higher value compared with the multi-pass coatings make the single-pass strategy more eligible for adoption in many cold spray aluminium alloy repair applications. The low porosity content of the coatings realized by the single-pass method is another important advantage of this deposition strategy. If better values for these parameters (adhesion and porosity) could be achieved by further optimization of the cold spray parameters or by implantation of new cold spray innovations (for example new nozzle designs or antisticking, water-cooled nozzles), the single-pass deposition strategy may give better results compared with the multi-pass approach. However, the multi-pass strategy with higher elastic modulus could be adopted in particular cases of repair where rigid reconstruction with a higher modulus is required, as in the surface of coupling flanges or in the edge of coupling mould shells.

Acknowledgments

The authors would like to acknowledge Matteo Mazucato, Veneto Nanotech laboratory chief technician, for his irreplaceable work and Mario Lamontagne, laboratory technician (CNRC), for his contribution.

References

1. V.K. Champagne, The Repair of Magnesium Rotorcraft Components by Cold Spray, *J. Fail. Anal. Prev.*, 2008, **8**, p 164-175
2. Q.C. Liu, P. Baburamani, W. Zhuang, D. Gerrard, B. Hinton, M. Janardhana, and K. Sharp, Surface Modification and Repair for Aircraft Life Enhancement and Structural Restoration, *Mater. Sci. Forum*, 2010, **654-656**, p 763-766
3. J.C. Lee, H.J. Kang, W.S. Chu, and S.H. Ahn, Repair of Damaged Mold Surface by Cold-Spray Method, *CIRP Ann. Manuf. Technol.*, 2007, **56**(1), p 577-580
4. Efforts to Reduce Corrosion on the Military Equipment and Infrastructure of the Department of Defense, Department of Defense Report, Office of the Secretary of Defense, June 2007
5. P. Fauchais and G. Montavon, Thermal and Cold Spray: Recent Developments, *Key Eng. Mater.*, 2008, **384**, p 1-59
6. S. Katsas, J. Nikolaou, and G. Papadimitriou, Microstructural Changes Accompanying Repair Welding in 5xxx Aluminium Alloys and Their Effect on the Mechanical Properties, *Mater. Des.*, 2006, **27**, p 968-975
7. S. Ignata, P. Sallamandb, D. Greveyb, and M. Lambertina, Magnesium Alloys Laser (Nd:YAG) Cladding and Alloying with Side Injection of Aluminium Powder, *Appl. Surf. Sci.*, 2004, **225**, p 124-134
8. R. Song, S. Hanaki, M. Yamashita, and H. Uchida, Reliability Evaluation of a Laser Repaired Die-Casting Die, *Mater. Sci. Eng. A*, 2008, **483-484**, p 343-345
9. K. Shankar and W. Wu, Effect of Welding and Weld Repair on Crack Propagation Behaviour in Aluminium Alloy 5083 Plates, *Mater. Des.*, 2002, **23**, p 201-208
10. S. Rech, A. Trentin, S. Vezzù, E. Irissou, J.G. Legoux, B. Arsenault, M. Lamontagne, C. Moreau, and M. Guagliano, Characterization of Residual Stresses in Al and Al/Al₂O₃ Cold Sprayed Coatings, *International Thermal Spray Conference & Exposition 2009*, May 4-7, 2009, ASM International, Las Vegas, Nevada, 2009, pp 1012-1017
11. A. Papyrin, V. Kosarev, S. Klinkov, A. Alkhimov, and V.M. Fomin, Chapter 4: Cold Spray Equipments and Technologies, *Cold Spray Technology*, 1st ed., Elsevier, Amsterdam, 2007, p 179-247
12. S. Rech, J.G. Legoux, E. Irissou, A. Trentin, S. Vezzù, and M. Guagliano, Influence of Pre-heated Al6061 Substrate Temperature on the Residual Stresses of Multi-pass Al-Coating Deposited by Cold Spray, *J. Therm. Spray Technol.*, 2011, **20**(1), p 243-251
13. Particle & Pore Analysis Module in SPIP, Image Metrology, <http://www.imagemet.com>
14. F. Kroupa, Residual Stresses in Thick, Non-homogenous Coating, *J. Therm. Spray Technol.*, 1997, **6**(3), p 147-150
15. E.F. Rybicki, R.T.R. McGrann, and J.R. Shadley, Applications and Theory of the Modified Layer Removal Method for the Evaluation of Through-Thickness Residual Stresses in Thermal Spray Coated Materials, *The Fifth Int. Conf. Residual Stresses*, ICRS-5, Linköping, 1997, p 994-999
16. M. Kulmala and P. Vuoristo, Influence of Process Conditions in Laser-Assisted Low-Pressure Cold Spraying, *Surf. Coat. Technol.*, 2008, **202**, p 4503-4508
17. S. Gulizia, A. Trentin, S. Vezzù, S. Rech, P. King, M. Jahedi, and M. Guagliano, Characterization of Cold Spray Titanium Coatings, *Mater. Sci. Forum*, 2010, **654-656**, p 898-901
18. T.H. Van Steenkiste, J.R. Smith, and R.E. Teets, Aluminum Coatings via Kinetic Spray with Relatively Large Powder Particles, *Surf. Coat. Technol.*, 2002, **154**, p 237-252
19. A.G. McDonald, A.N. Ryabinin, E. Irissou, and J.-G. Legoux, Gas-Substrate Heat Exchange During Cold-Gas Dynamic Spraying, *J. Therm. Spray Technol.*, 2013, **22**(2-3), p 391-397
20. Heat Treating, *ASM Handbook, Edition Metals Handbook*, vol. 4, 1990, p 1872-2173
21. J.M. Berthelot and L. Fatmi, Statistical Investigation of the Fracture Behavior of Inhomogeneous Materials in Tension and Three-Point Bending, *Eng. Fract. Mech.*, 2004, **71**, p 1535-1556
22. A.G. Evans and R.M. McMeeking, On the Toughening of Ceramics by Strong Reinforcements, *Acta Metall.*, 1986, **34**, p 2435-2441
23. M. Watanabe, M. Komatsu, and S. Kuroda, Multilayered WC-Co/Cu Coatings by Warm Spray Deposition, *Surf. Coat. Technol.*, 2011, **205**(23-24), p 5358-5368
24. Fatigue and Fracture, *ASM Handbook, Edition Metals Handbook*, vol. 19, 1990, p 2324-2363